Journal of Power Sources 195 (2010) 834–844

Contents lists available at ScienceDirect

Journal of Power Sources

journal homepage: www.elsevier.com/locate/jpowsour

Fe content effects on electrochemical properties of Fe-substituted Li_2MnO_3 positive electrode material

Mitsuharu Tabuchi[a,*], Yoko Nabeshima[a], Tomonari Takeuchi[a], Kuniaki Tatsumi[a], Junichi Imaizumi[b], Yoshiaki Nitta[b]

[a] National Institute of Advanced Industrial Science and Technology (AIST), 1-8-31 Midorigaoka, Ikeda, Osaka 563-8577, Japan
[b] Tanaka Chemical Corporation, 5-10 Shirakata-cho, Fukui 910-3131, Japan

ARTICLE INFO

Article history:
Received 19 May 2009
Received in revised form 23 August 2009
Accepted 24 August 2009
Available online 31 August 2009

Keywords:
Rechargeable lithium battery
Positive electrode material
Lithium transition metal oxide
Wet-chemical preparation method

ABSTRACT

Fe-substituted Li_2MnO_3 including a monoclinic layered rock-salt structure ($C2/m$), $(Li_{1+x}(Fe_yMn_{1-y})_{1-x}O_2$, $0<x<1/3$, $0.1\leq y\leq 0.5$) was prepared by coprecipitation–hydrothermal–calcination method. The sample was assigned as two-phase composite structure consisting of the cubic rock-salt ($Fm\bar{3}m$) and monoclinic ones at high Fe content above 30% ($y\geq 0.3$), while the sample was assigned as a monoclinic phase ($C2/m$) at low Fe content less than 20%. In the monoclinic Li_2MnO_3-type structure, the Fe ion tends to substitute a Li ($2b$) site, which corresponds to a center position of Mn^{4+} hexagonal network in Mn–Li layer. The electrochemical properties including discharge characteristics under high current density (<3600 mA g^{-1} at 30 °C) and low temperature (<−20 °C at 40 mA g^{-1}) were severely affected by chemical composition (Fe content and Li/(Fe + Mn) ratio), crystal structure (monoclinic phase content) and powder property (specific surface area). Under the optimized Fe content ($0.2<y<0.4$), the Li/sample cells showed high initial discharge capacity (240–300 mAh g^{-1}) and energy density (700–950 mWh g^{-1}) between 1.5 and 4.8 V under moderate current density, 40 mA g^{-1} at 30 °C. Results suggest that Fe-substituted Li_2MnO_3 would be a non-excludable 3 V positive electrode material.

1. Introduction

Lithium-ion batteries are now an attractive power source used in many laptop computers and cellular telephones. Their application will extend to hybrid and electric vehicles because of their high energy density and long life. Among their constituent materials, the selection of positive electrode active material are important because the cell capacity and voltage depend predominantly on the electrochemical performance of positive electrode material. Especially, the choice of positive electrode material with high Li content is one of effective ways to increase the cell capacity.

Lithium transition metal oxides with high Li contents like Li_2MnO_3 [1–3] and its derivatives [4–7] are therefore attractive candidates. If all lithium from Li_2MnO_3 were extracted and inserted electrochemically, the ideal specific capacity (Q) could reach 460 mAh g^{-1}, which exceeds that of present positive electrode materials like $LiCoO_2$ (ca. 270 mAh g^{-1}). Especially, a Li_2MnO_3–$LiMO_2$ (M = Cr [4], Co [5] and Ni [6,7]) solid solution is a main target material for study because of its lack of initial cycle efficiency and cycle stability at room temperature for Li_2MnO_3 [1–3]. Although the importance of substitution of other 3d transition metals for manganese is well known, the transition metal substitution effect on electrochemical properties of Li_2MnO_3-based electrode materials remains unknown in spite of energetic study of Cr [8,9], Co [10], Ni [11–13] or Co and Ni [14–17] substituted Li_2MnO_3. The difficulty arises from inhomogeneous distribution of host Mn ion and guest cations into the layered rock-salt structure. Therefore, electrochemical properties of Li_2MnO_3–$LiMO_2$ solid solution were severely affected by the sample preparation history. We noticed that samples with different degrees of Fe substitution should be prepared under an optimized preparation condition and sample nature parameters like chemical composition, crystal structure and powder property need to be compared carefully with electrochemical data for overcoming this problem.

Investigations by our group found that Li_2MnO_3–$LiFeO_2$ solid solution (Fe-substituted Li_2MnO_3, $Li_{1+x}(Fe_yMn_{1-y})_{1-x}O_2$, $0<x<1/3$, $0<y<1$) [18–21] can behave as a 4 V positive electrode material when the upper voltage limit was adjusted less than 4.3 V. It has high specific capacities (>200 mAh g^{-1}) with acceptable average voltage (3 V) was obtained when one positive electrode materials ($Li_{1.2}Fe_{0.4}Mn_{0.4}O_2$) is cycled between 2.0 and 4.5 V at 60 °C [22,23]. The high specific capacity cannot be explained merely by oxidation of all trivalent Fe ions and subsequent reduction because the ideal capacity is limited

* Corresponding author. Tel.: +81 727 51 9618; fax: +81 727 51 9714.
E-mail address: m-tabuchi@aist.go.jp (M. Tabuchi).

0378-7753/$ – see front matter © 2009 Elsevier B.V. All rights reserved.
doi:10.1016/j.jpowsour.2009.08.059

to 127 mAh g^{-1}. We clarified that its high Li content and small particle size of less than 100 nm were responsible for the high initial specific capacity [22,23]. Consideration from the perspective of crystal structure is needed because $Li_{1.2}Fe_{0.4}Mn_{0.4}O_2$ possesses a two-phase nature: layered ($R\bar{3}m$) and cubic ($Fm\bar{3}m$) rock-salt structures [22,23]. Former and latter ones were assigned as Fe-substituted Li_2MnO_3 and Mn-substituted $LiFeO_2$ [22,23]. Kikkawa et al. analyzed this sample using analytical transmission electron microscopy (TEM) and found that rock-salt phases of two kinds coexist within one particle and that the intergrowth structure appeared because of inhomogeneous distribution of Fe and Mn ions [24,25]. Recently, they succeeded in visualizing the Li ion distribution in a particle, which revealed that the initial delithiation process start from Mn-substituted $LiFeO_2$ domain (<50% of state of charge (SOC)) and propagate through the rest (Fe-substituted Li_2MnO_3) up to 100% of SOC and that oxygen loss occurred in both Mn-rich and Fe-rich nanodomains at the 100% of SOC [26]. The initial charge mechanism is consistent with the previous results of Li_2MnO_3–LiMO_2 solid solution [16] and theoretical and experimental evidence of Li_2MnO_3 [27,28]. The result means that $LiFeO_2$ domain can facilitate the Li extraction from Li_2MnO_3. Valence state analysis of Fe ion was performed for the 30% Fe-substituted Li_2MnO_3 ($Li_{1+x}(Fe_{0.3}Mn_{0.7})_{1-x}O_2$) using ^{57}Fe Mössbauer spectroscopy. Extremely high oxidation states of iron ions such as tetravalent and pentavalent states were found in the cation-ordered Li_2MnO_3 structure [29] without chemical or electrochemical oxidation. In spite of these previous approaches, a method of optimizing the electrochemical property for this material remains unknown.

For this study, we prepare this material with different Fe contents of 10–50% under the same preparation conditions to determine the sample nature parameters responsible for electrochemical properties below room temperature, including discharge characteristics, under a high current density up to 3600 mA g^{-1} at +30 °C and moderate current density (40 mA g^{-1}) at −20 °C.

2. Experimental

All samples $Li_{1+x}(Fe_yMn_{1-y})_{1-x}O_2$ ($0 < x < 1/3, 0.1 \le y \le 0.5$), were prepared using the coprecipitation–hydrothermal–calcination method (0.25 mol/batch) [23]. Five samples with different Fe contents (y) of 0.1–0.5 were designated as Samples Y01–Y05 corresponding to their y values. The Fe content was controlled by changing the mixing ratios of starting materials: $Fe(NO_3)_3{\cdot}9H_2O$ and $MnCl_2{\cdot}4H_2O$. The heat-treatment condition is fixed at 850 °C for 1 min in air and 1 h is taken for heating samples for approaching the target temperature.

The samples are characterized by X-ray diffraction (XRD) pattern measurements as well as Li, Fe, and Mn elemental analysis using inductively coupled plasma (ICP) emission spectroscopy and average valence state analysis of transition metals through iodometric titration. For X-ray Rietveld analysis, Si powder (SRM 640c) was used as an external standard for calibrating the diffraction angle. The XRD data were collected between 10° and 125° of the 2θ angles under monochromatized Cu Kα radiation using an X-ray diffractometer (Rotaflex RU-200B/RINT; Rigaku Corp.). A split pseudo-Voigt profile function was selected for each XRD peak fitting. A computer program, RIETAN-2000 [30], was used for X-ray Rietveld analysis. The particle shape and size were checked using scanning electron microscopy (SEM, JSM-6390; JEOL) with a LaB_6 filament. The Brunauer–Emmett–Teller (BET) surface area was measured and used as specific surface area (SSA) data.

A coin-type lithium half-cell was used to examine cell properties. A positive electrode was made from 5 mg of active material, 5 mg of acetylene black, and 0.5 mg of polytetrafluoroethylene (PTFE) powder. Aluminum mesh was selected as the current collector of the positive electrode; Li metal was used as a negative electrode. A typical organic electrolyte, $LiPF_6$, was selected for cell tests. It was dissolved in mixed solvent, ethylene carbonate (EC) and dimethylcarbonate (DMC). Cell tests started from charging greater than 4.8 V under moderate current density per unit of mass of the active material, 40 mA g^{-1}, and discharged to 1.5 V at the same current density after charging, unless otherwise specified. Most cell tests were performed at 30 °C. Two initial charge procedures were tested for the charge–discharge cycle performance; (1) a cell was charged up to 4.8 V with a 40 mA g^{-1} of current density and then this voltage was fixed under decreasing current density to 2 mA g^{-1}; (2) a cell was charged to less than 5.5 V with a 40 mA g^{-1} of current density up to 500 mAh g^{-1} less than 5.5 V. To evaluate the initial cycle efficiency and maximum discharge capacity properly, the former and latter charge modes were selected, respectively.

The discharge characteristics at +30 °C under various current densities were evaluated from 40 to 3600 mA g^{-1} between 1.5 and 4.8 V after charging at 40 mA g^{-1}. The cell was charged to 4.8 V; then the cell voltage was kept at 4.8 V until lowering current density to 2 mA g^{-1} only during initial charging. One cycle test under moderate current density (40 mA g^{-1}) was added before correcting each discharge data at desired current density. The discharge behavior at 0 and–20 °C was collected at a fixed current density, 40 mA g^{-1} after charging at +30 °C. In the initial charging run, the cell was charged less than 5.5 V at 40 mA g^{-1} to reach 500 mA g^{-1}. One cycle test under the same current density (40 mA g^{-1}) at 30 °C was added before examining each low-temperature property.

3. Results and discussion

3.1. Structure, chemical composition, and particle size of samples

The XRD patterns of all samples are presented in Fig. 1. All XRD peaks were indexed by the monoclinic unit cell of Li_2MnO_3 ($C2/m$ [31]). No impurity phases like Li_2CO_3, $LiMnO_2$ and α-$LiFeO_2$ were detected. The orthorhombic $LiMnO_2$ was formed during the preparation of non-doped Li_2MnO_3. Therefore non-doped Li_2MnO_3 cannot be used as a reference sample. The XRD pattern analysis will be described later in detail.

The elemental analysis data (Table 1) depict that observed Fe/(Fe + Mn) ratios (y in $Li_{1+x}(Fe_yMn_{1-y})_{1-x}O_2$) agree with the nominal ratio, as described in Section 2, indicating the easy control of transition metal ratio by our preparation method. The Li/(Fe + Mn) ratio and x value decreased with increasing Fe content, as expected

Table 1
Elemental analysis and BET surface area (SSA) values for the $Li_{1+x}(Fe_yMn_{1-y})_{1-x}O_2$ samples with different Fe contents y.

Sample	SSA/(m^2 g^{-1})	Li/wt%	Fe/wt%	Mn/wt%	Li/(Fe + Mn)	$Li_{1+x}(Fe_yMn_{1-y})_{1-x}O_2$	
						x	y
Sample Y01	16.4	11.1	4.8	40.8	1.92	0.32	0.10
Sample Y02	20.4	10.4	9.7	37.2	1.77	0.28	0.20
Sample Y03	22.1	10.1	14.7	34.1	1.65	0.25	0.30
Sample Y04	19.8	9.9	19.9	29.3	1.60	0.23	0.40
Sample Y05	16.7	9.5	25.1	24.4	1.53	0.21	0.50

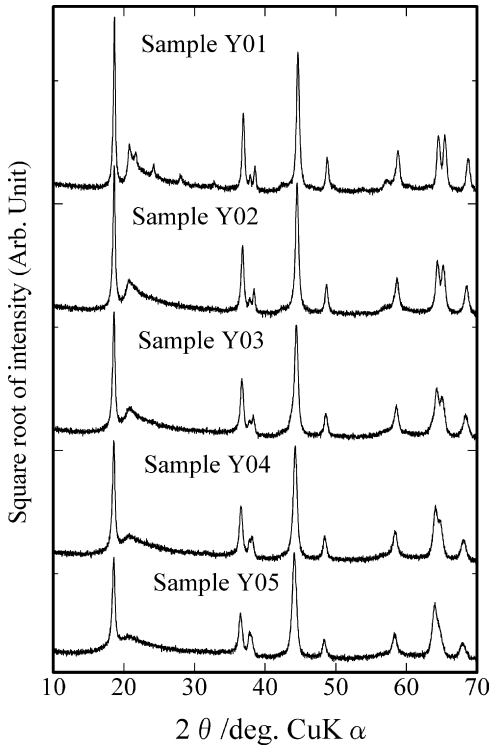

Fig. 1. X-ray diffraction (XRD) patterns of Samples Y01–Y05 with different iron contents to the total transition metal contents of 10–50%. The vertical axis was converted to a square root scale for detecting superstructure peaks with small intensity between 20° and 35°.

from the sample nature; the Fe-substituted Li_2MnO_3 is considered as the yLiFeO$_2$–$(1-y)$Li$_2$MnO$_3$ solid solution. The average oxidation state of transition metal ions in Sample Y05 was 3.46, which is close to the expected value (3.50) constructed from the chemical formula of $Li_{1.2}Fe_{0.4}Mn_{0.4}O_2$ (0.5LiFeO$_2$–0.5Li$_2$MnO$_3$). These results show that the chemical composition of our sample is lying on the LiFeO$_2$–Li$_2$MnO$_3$ solid solution. The specific surface area (SSA) value has a maximum at $y = 0.3$ (Sample Y03) as a function of Fe content, which suggests that Samples Y04 and Y05 have a different sample nature from the others. The difference in sample nature will be discussed in the X-ray Rietveld analysis part.

For structural refinement using the X-ray Rietveld analysis, we select a monoclinic Li$_2$MnO$_3$-type model ($C2/m$) instead of hexagonal LiCoO$_2$-type one ($R\bar{3}m$) as a major phase, based on two results: (1) the existence of superstructure peaks was within the 2θ range of 20–35° for Sample Y01 as shown in Fig. 1; and (2) such superstructure peaks were observed even at the maximum Fe content (50%) through electron diffraction analysis using analytical TEM for Sample Y05 [25]. The superstructure peaks originate from the existence of honeycomb ordering of transition metal ion into Li–Mn layer of Li$_2$MnO$_3$ structure [11,31], which will be shown in Fig. 4(b). Fitting result for Sample Y01 was depicted in Fig. 2, indicating that all of XRD peaks were fitted well using the unit cell of Li$_2$MnO$_3$ ($C2/m$). We apply a two-phase model including cubic α-LiFeO$_2$-type structure [32] ($Fm\bar{3}m$) as the minor phase for Samples Y03–Y05, as presented in Table 2 because of the asymmetric nature of XRD peaks around $2\theta = 43°$ and 64° and previous results [22–25]. Although Samples Y03–Y05 are intergrowth two-phase structures [24,25], Samples Y01 and Y02 with low Fe contents are the single monoclinic phase. That fact indicates that the solubility limit of Fe ion into Li$_2$MnO$_3$ structure is close to 20% of the total transition metal content under a present preparation condition. The low Fe solubility limit might explain the Fe content dependence of specific surface area having a maximum around 30%. Although the grain growth of

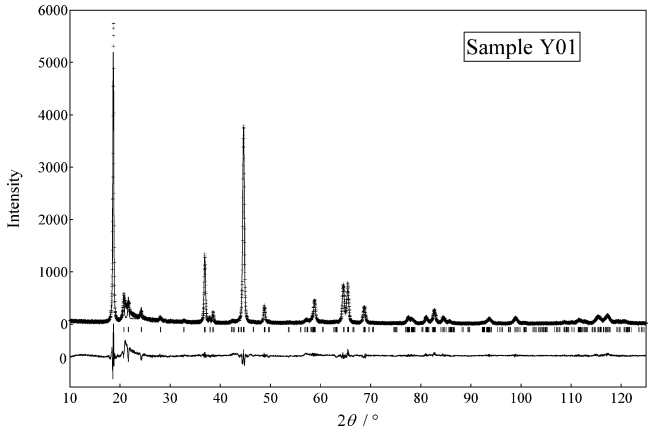

Fig. 2. Observed (+) and calculated (solid line) XRD patterns for Sample Y01. The calculated patterns were constructed from a unit cell of monoclinic Li$_2$MnO$_3$ with $C2/m$ of space groups.

Li$_2$MnO$_3$ particles is suppressed by incorporation of foreign Fe ion less than 20%, constituent particles of samples with high Fe content greater than 40% become large by two-phase separation to Fe-substituted Li$_2$MnO$_3$ and Mn-substituted LiFeO$_2$ nanodomains. Further improved preparation techniques are needed to obtain a homogeneous sample with high Fe contents.

Because the specific surface area is proportionate to the reciprocal number of primary particle size in general, difference in particle size among samples were checked, as depicted in Fig. 3. All samples consisted of agglomerated particles of submicrometer diameter to a hundred micrometer diameter. The SEM photographs correspond to the surface of agglomerated particles. Although all samples consist of fine particles smaller than 100 nm (0.1 μm), as expected from the SSA values, no systematic change in particle size was detected by SEM observation.

The lattice volumes for both monoclinic and cubic phases increased with increasing Fe content, as presented in Table 2(a). The fact suggests that Fe substitution for Mn and Li ions continued at both phases with increasing Fe contents greater than 30% after two-phase separation. The cubic phase content increased with increasing Fe content, indicating that an incomplete cation mixing state was stabilized at greater than 30% of Fe contents.

Transition metal contents per chemical formula (M), $Li_{1+x}M_{1-x}O_2$ (Table 2(b)) reflects its average valence state because the chemical formula is respectively changeable from LiMO_2 ($x = 0$, $M = 1.00$) to $Li_{4/3}M_{2/3}O_2$ (Li$_2MO_3$, $x = 1/3$, $M = 0.67$) depending on the average valence state from 3+ to 4+, respectively. The M values of monoclinic and cubic phases were 0.64–0.81 and 0.63–0.86, which are lying on expected ones of $Li_{4/3}M_{2/3}O_2$–LiMO_2 solid solution. The results indicate that the both of monoclinic and cubic phases contain trivalent Fe and tetravalent Mn ions as expected from the iodometric titration result of Sample Y05, previous Mn and Fe K-edge XANES and ^{57}Fe Mössbauer spectra [22], and analytical TEM results [24,25].

As portrayed in Fig. 4, four crystallographic sites––2b, 2c, 4g, and 4h sites––allow for occupation by cations of the monoclinic Li$_2$MnO$_3$ structure [31]. In the ideal Li$_2$MnO$_3$ structure, Mn^{4+} ions occupy only the 4g site; Li^+ ions exist at three residual sites. However, the Mn ion occupancy at 4g sites was less than 100% because of the existence of Mn ion disordering [31]. In fact, transition metal occupancy data of 4g sites for all samples were less than unity (0.55–0.73), as presented in Table 2(b). Most transition metal ions exist on 4g and 2b sites, which create Li–Mn layers, as portrayed in Fig. 4(b). The transition metal ions tend to occupy on 2c site rather than 4h site in the Li layer. The transition metal occupancy on Li layer ($(2g_{4h} + g_{2c})/3$) (Table 2(b)) increased with Fe content.

Table 2
X-ray Rietveld refinement results for the $Li_{1+x}(Fe_yMn_{1-y})_{1-x}O_2$ samples with different Fe contents y.

Sample	Monoclinic Li_2MO_3 ($C2/m$) phase						Cubic $LiMO_2$ ($Fm\bar{3}m$) phase		
	Fraction/%	a/Å	b/Å	c/Å	β/°	V/Å^3	Fraction/%	a/Å	V/Å^3
(a) Fractions and lattice parameters of monoclinic Li_2MO_3 and cubic $LiMO_2$ phases									
Sample Y01	100	4.9418 (12)	8.5445 (14)	5.0195 (8)	109.188 (19)	200.17 (5)	–	–	–
Sample Y02	100	4.9580 (13)	8.5679 (16)	5.0265 (9)	109.14 (2)	201.72 (7)	–	–	–
Sample Y03	81	4.9704 (14)	8.5750 (18)	5.0364 (11)	109.12 (2)	202.81 (8)	19	4.0752 (17)	67.68 (5)
Sample Y04	79	4.9881 (18)	8.608 (2)	5.0459 (13)	109.26 (3)	204.52 (10)	21	4.0951 (12)	68.68 (4)
Sample Y05	71	4.9938 (17)	8.601 (2)	5.0392 (13)	109.31 (3)	204.28 (10)	29	4.1033 (6)	69.088 (18)

Sample	Monoclinic Li_2MO_3 ($C2/m$) phase							Cubic $LiMO_2$ ($Fm\bar{3}m$) phase	
	Transition metals in a Li layer			Transition metals in a Li–Mn layer					
	g_{2c} ($2c$ site)	g_{4h} ($4h$ site)	$(2g_{4h}+g_{2c})/3$	g_{4g} ($4g$ site)	g_{2b} ($2b$ site)	$(2g_{4g}+g_{2b})/3$	M in $L_{1+x}M_{1-x}O_2$	g_{4a} ($4a$ site)	M in $L_{1+x}M_{1-x}O_2$
(b) Occupancy (g) of transition metal for each crystallographic site, calculated transition metal contents in Li ($(2g_{4h}+g_{2c})/3$) and Li–Mn layers ($(2g_{4g}+g_{2b})/3$, see Fig. 4(a)) and transition metal content per chemical formula (M) for monoclinic Li_2MO_3 and cubic $LiMO_2$ phases									
Sample Y01	0.012 (5)	0.038 (4)	0.029 (5)	0.733 (6)	0.390 (6)	0.619 (6)	0.648 (11)	–	–
Sample Y02	0.113 (6)	0.038 (4)	0.063 (5)	0.567 (4)	0.749 (8)	0.628 (5)	0.691 (10)	–	–
Sample Y03	0.093 (10)	0 (fixed)	0.031 (3)	0.548 (10)	0.729 (18)	0.608 (13)	0.639 (16)	0.431 (19)	0.86 (4)
Sample Y04	0.258 (9)	0 (fixed)	0.086 (3)	0.693 (9)	0.727 (13)	0.704 (11)	0.790 (14)	0.314 (14)	0.63 (3)
Sample Y05	0.290 (9)	0 (fixed)	0.097 (3)	0.692 (8)	0.765 (13)	0.716 (10)	0.813 (13)	0.345 (8)	0.690 (16)

Imaginary transition metals ($M = Fe_yMn_{1-y}$) share the same crystallographic site with Li; the sum of the M and Li occupancies was fixed at unity for all sites.
Occupancy of $4h$ and $2c$ sites was fixed at zero when negative values were observed during fitting.
The M values are calculated by the sum of two kinds of transition metal contents in Li and Li–Mn layers such as $(2g_{4h}+g_{2c})/3$ and $(2g_{4g}+g_{2b})/3$, respectively, for the monoclinic phase, and the M values correspond to $2g_{4a}$ for the cubic phase.

The trend means that stabilization of disordered layered rock-salt structure by Fe substitution, which may impede fast Li diffusion in monoclinic phase during charge and discharge tests, especially for Samples Y04 and Y05.

Samples Y02–Y05 had a unique cation distribution observed for the monoclinic phase. In the ideal Li–Mn layer of Li_2MnO_3 structure, the Mn ion on the $4g$ site creates a hexagonal network, although the Li ion in $2b$ site exists at the center position of each Mn hexagon, as portrayed in Fig. 4(b). If the Fe ion has neither $4g$ nor $2b$ site preference, the occupancy of the $4g$ site is always higher than that of $2b$ site, engendering the disordered hexagonal network structure. Although Sample Y01 has the disordered hexagonal network structure as shown in Table 2(b), the rest have an inverse hexagonal network structure, for which the $2b$ site occupancy is higher than the $4g$ site one. Such a unique cation distribution is constructed by strong $2b$ site preference of Fe ion in the monoclinic Li_2MnO_3 structure. The $2b$ site preference tendency of Fe ion is similar to the site preference of other 3d cations such as Ni^{2+}, Ni^{3+} and Co^{3+} [33]. Although the above fitting result is predictable from previous data [33], X-ray pattern fitting using the monoclinic unit cell ($C2/m$) have an advantage compared to selecting hexagonal unit cell ($R\bar{3}m$) because of possible characterization about cation distribution of Li–M layer in the layered rock-salt structure.

Fig. 5 showed plots of sample nature parameters against Fe content (Fe/(Fe + Mn) ratio). Li/(Fe + Mn) ratio decreased monotonously with increasing Fe content as well as monoclinic phase content, while specific surface area (SSA) data have a maximum at 30% of Fe content. The result means that Li/(Fe + Mn) ratio and monoclinic phase content are difficult to treat as independent parameters each other. The analyses of chemical composition, crystal structure and powder nature of these samples are used for interpreting the Fe content dependence of electrochemical data in the next part.

3.2. Electrochemical properties of samples

Initial charge curves above 3.8 V were shown in Fig. 6(a). As expected from previous charge curves of $LiMO_2$–Li_2MnO_3 solid solution (M = Co [10], $Ni_{1/2}Mn_{1/2}$ [11] or $Ni_{1/3}Mn_{1/3}Co_{1/3}$ [15]), two different plateaus were observed below and above 4.4 V. The charge curves below and above 4.4 V have been attributed to Li extraction from $LiMO_2$ component and Li_2O extraction from Li_2MnO_3 component, respectively [13,16,34]. Although initial charge capacity below 4.4 V increased with increasing Fe content, those above 4.4 V decreased. The trend lead to a conclusion that initial charge capacity below and above 4.4 V can be assigned to Li extraction from Mn-substituted $LiFeO_2$ ($Fm\bar{3}m$) and Li_2O extraction from Fe-substituted Li_2MnO_3 ($C2/m$) components, respectively. The initial charge mechanism is consistent with our previous result using analytical TEM, which Li extraction start from Fe-rich domain (Mn-substituted $LiFeO_2$) to Mn-rich one (Fe-substituted Li_2MnO_3) and oxygen loss was observed at the end of charging for $Li_2(Fe_{0.5}Mn_{0.5})_{0.8}O_2$ [26]. Interestingly, the voltage plateau region above 4.4 V shift toward to lower voltage region with increasing Fe content. The change is one of important effect of Fe substitution.

The Fe content also affected the initial discharge curve profile as shown in Fig. 6(b). Smooth downslope profile until 3.0 V was obtained for Samples Y01 and Y02 positive electrodes. The discharge curves bent around 3.5 V for Samples Y03, Y04 and Y05 positive electrodes and the bending appeared clearly with increasing Fe content. Although the origin of bending point around 3.5 V is still unknown, initial discharge curves may depending on the chemical composition (Fe/(Fe + Mn) and Li/(Fe + Mn) ratios) and/or the monoclinic/cubic phase ratio as denoted in Fig. 5. Careful structural or compositional analyses are needed to know the complex initial charge and discharge mechanism using two or more samples with different Fe content.

Initial, 2nd, and 20th charge and discharge curves for Li/sample cells are presented in Fig. 7. Although the initial charge and discharge capacities decreased with increasing Fe content, the initial cycle efficiency was improved. When the Fe content (Fe/(Fe + Mn) ratio) is adjusted to less than 20%, the initial discharge capacity and energy density reach 300 mAh g^{-1} and 900 mWh g^{-1} (see Table 3(a)), respectively. The high capacity and energy density denotes that Fe-substituted Li_2MnO_3 is an attractive candidate as well as other Li_2MnO_3-based positive electrode materials. The profile of 2nd charge curve is quite different from that of initial one and is regarded as a symmetric shape of 1st discharge one, suggesting that the plateau around 4.5 V considered as Li_2O extraction process [3,13,16,34] was almost finished at the end of 1st charging as well as other Li_2MnO_3-based materials.

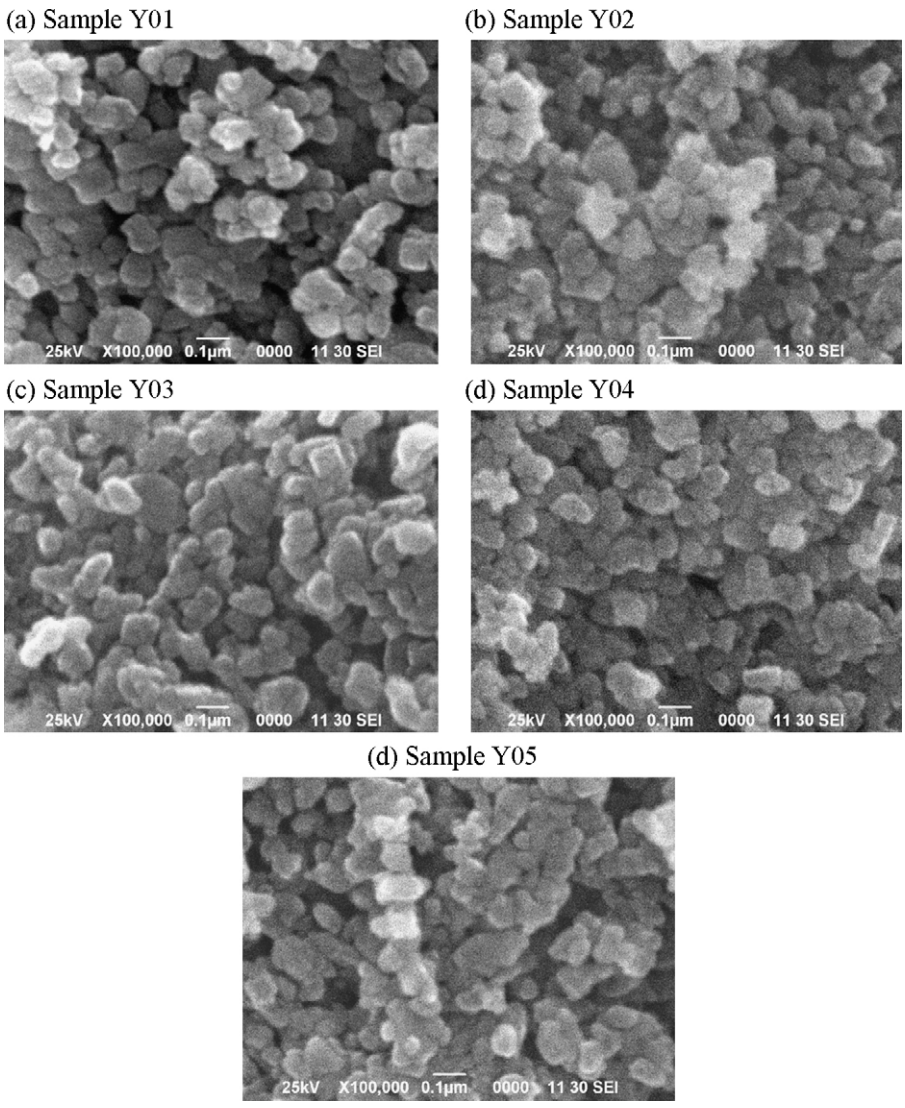

Fig. 3. Scanning electron microprobe (SEM) images for Samples Y01–Y05. The same magnification was selected for direct comparison. Length of white bar in each photograph is 0.1 μm.

Table 3
Electrochemical charge and discharge characteristics for Li/sample cells at 30 °C.

Sample	Q_{1c}/(mAh g^{-1})	Q_{1d}/(mAh g^{-1})	Q_{1d}/Q_{1c}	V_{ave}/V	$V_{ave}\cdot Q_{1d}$/(mWh g^{-1})	Q_{20d}/(mAh g^{-1})	Q_{20d}/Q_{1d}
(a) Data of cells operated between 1.5 and 4.8 V under a fixed current density, 40 mA g^{-1}. Charging remained at the upper limit voltage until reducing the current density to 2.0 mA g^{-1} only during the initial charging run							
Sample Y01	500	312	0.63	2.96	924	188	0.60
Sample Y02	425	299	0.70	2.98	891	200	0.67
Sample Y03	409	265	0.65	2.96	784	186	0.70
Sample Y04	356	241	0.68	2.96	713	188	0.78
Sample Y05	356	264	0.74	2.88	761	183	0.69
Sample	Q_{1c}/(mAh g^{-1})	Q_{1d}/(mAh g^{-1})	Q_{1d}/Q_{1c}	V_{ave}/V	$V_{ave}\cdot Q_{1d}$/(mWh g^{-1})	Q_{20d}/(mAh g^{-1})	Q_{20d}/Q_{1d}
(b) Data of cells operated between 1.5 and 4.8 V under a fixed current density, 40 mA g^{-1}. Charging was maintained at 500 mAh g^{-1} under the same current density only during the initial charging run							
Sample Y01	500	321	0.64	3.02	971	199	0.62
Sample Y02	500	307	0.61	2.97	911	201	0.65
Sample Y03	500	285	0.57	2.98	850	194	0.68
Sample Y04	500	265	0.53	2.95	782	185	0.70
Sample Y05	500	261	0.52	2.94	767	180	0.69

Q_{1c}, initial charge capacity; Q_{1d}, initial discharge capacity; Q_{1d}/Q_{1c}, initial efficiency; V_{ave}, average voltage; $V_{ave}\cdot Q_{1d}$, initial discharge energy density; Q_{20d}, 20th discharge capacity.
Q_{1c}, initial charge capacity; Q_{1d}, initial discharge capacity; Q_{1d}/Q_{1c}, initial efficiency; V_{ave}, average voltage; $V_{ave}\cdot Q_{1d}$, initial discharge energy density; Q_{20d}, 20th discharge capacity.

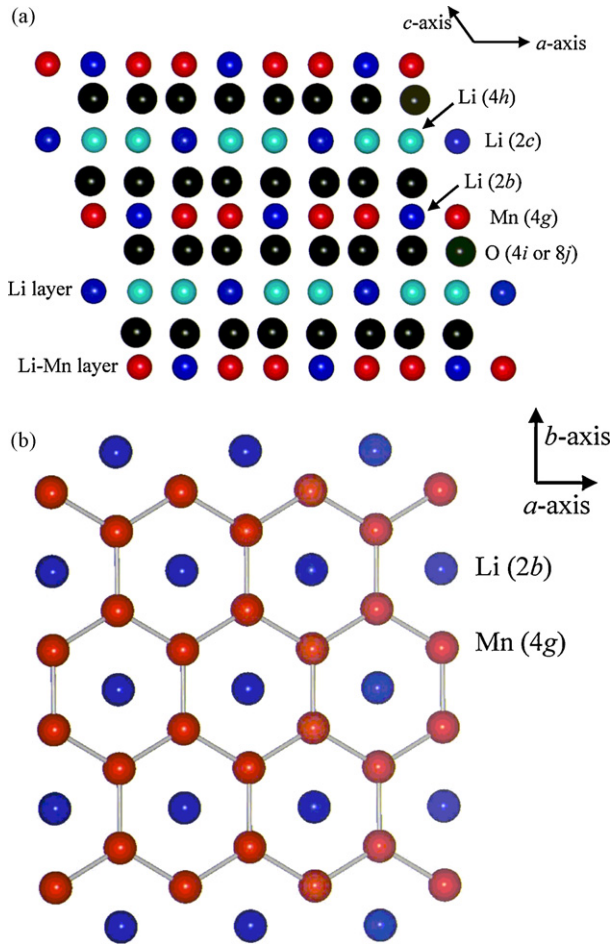

Fig. 4. Li, Mn, and O arrangements in Li_2MnO_3 (*C*2/*m*) proposed by Strobel and Lambert-Andron [31]. In (a), Li_2MnO_3 consists of alternative stacking of Li and Li–Mn layers via an oxide ion layer comprising crystallographic sites of two kinds (4*i* and 8*j* sites). Each cation layer consists of 2*c* and 4*h* sites for the Li layer and 4*g* and 2*b* sites for the Li–Mn layer. In (b), the cation arrangement in the Li–Mn layer is represented as a hexagonal Mn network and Li ions existing at the center position of the hexagonal network to make Mn_6Li cluster.

The additional discharge plateau around 2.0–2.5 V was appeared for 20th cycle curves of Samples Y01 and Y02 and was not observed for the rest three samples with relatively high Fe content above 30%. Although the origin of the plateau that appeared remains unknown, the discharge curve shapes resemble that of the Li_2MnO_3–$Li_4Mn_5O_{12}$ composite material [35]. The change in shape suggests that spinel-like oxide was formed gradually with proceeding charge–discharge cycles. The conversion from a layered rock-salt phase to a spinel one during electrochemical cycle tests was reported for not only Li_2MnO_3 [36] but also $LiCoO_2$–Li_2MnO_3 solid solution [10,37]. The formation of "$LiMnO_2$" component is one of reason for the conversion because $LiMnO_2$ undergo a structural change to spinel during electrochemical cycling [38]. The $LiMnO_2$ content per chemical formula increased with increasing the capacity of the Li_2O extraction from Li_2MnO_3 component on initial charging [3,16]. Appearance of the additional plateau was suppressed by increasing Fe content greater than 30% (Samples Y03–Y05) and by reducing the capacity of high voltage plateau above 4.4 V (see Fig. 6(a)). The stabilization of charge and discharge curve profile during electrochemical cycling can be attributed to a merit of Fe incorporation into Li_2MnO_3 as well as Ni incorporation [7].

Discharge capacity sustainability (Q_d/Q_{1d}) with cycle number was plotted in Fig. 8. The capacity fading up to 20th cycle was sup-

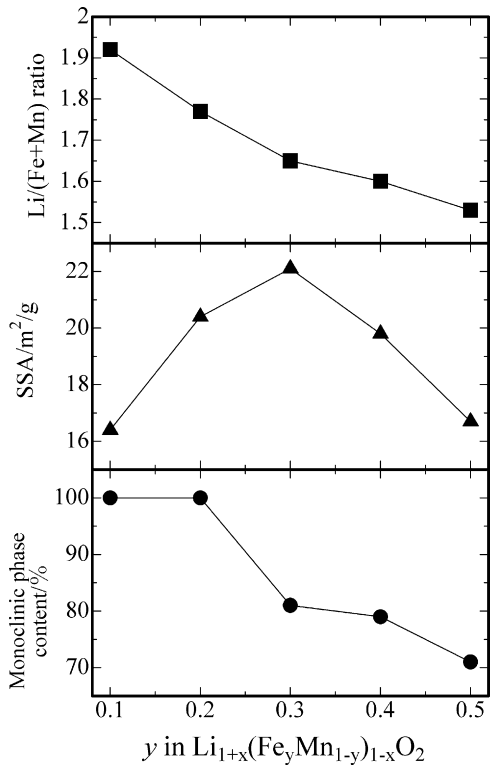

Fig. 5. The Fe content dependence on Li/(Fe + Mn) ratio, BET specific surface area (SSA) and monoclinic phase content data for Samples Y01–Y05.

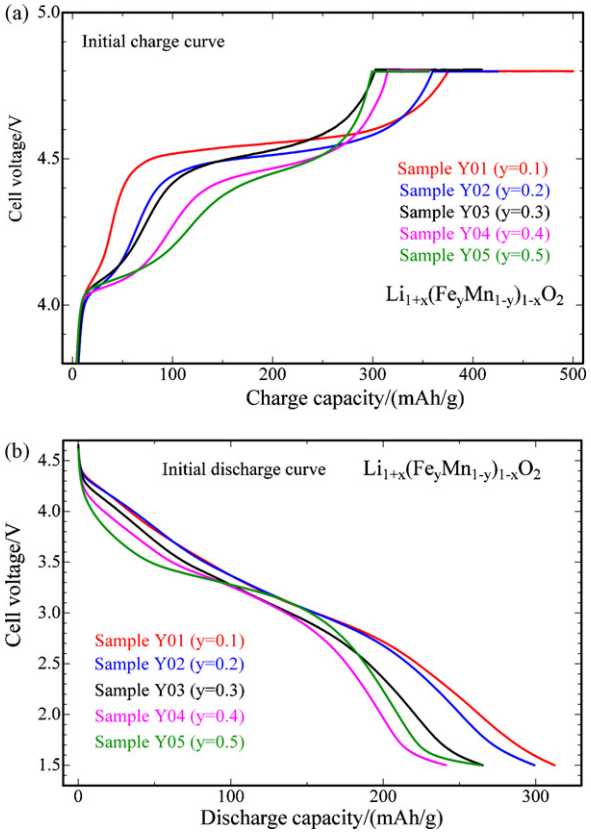

Fig. 6. Initial charge (a) and discharge (b) curves at 30 °C of Li/Sample Y01–Y05 cells for 1.5–4.8 V under a fixed current density, 40 mA g^{-1}. The cell voltage was fixed at the upper voltage limit with decreasing current density until 2 mA g^{-1} only during the initial charging run.

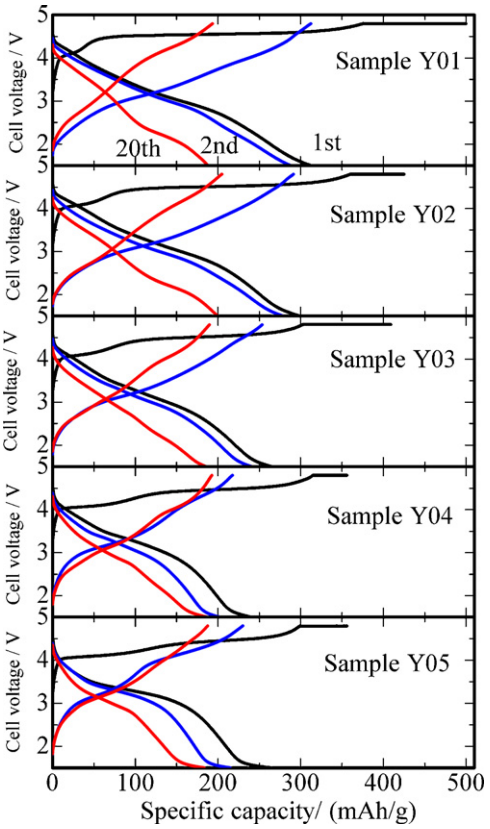

Fig. 7. Initial (black), 2nd (blue), and 20th (red) charge and discharge curves at 30 °C of Li/Sample Y01–Y05 cells for 1.5–4.8 V under a fixed current density, 40 mA g^{-1}. The cell voltage was fixed at the upper voltage limit with decreasing current density until 2 mA g^{-1} only during the initial charging run. (For interpretation of the references to color in this figure legend, the reader is referred to the web version of the article.)

pressed from 40 to 20% with increasing Fe content. Although the change in Q_d/Q_{1d} values for Samples Y04 and Y05 after 2nd cycle is quite small compared to those of other samples, drastic capacity fading behavior above 15% was observed from 1st to 2nd cycles for the two samples. To minimize such capacity fading is one of important research topics.

The charge–discharge behavior was checked after charging until 500 mAh g^{-1} per mass of the sample. Although the initial discharge capacity was increased (10–25 mAh g^{-1}) slightly as listed in Table 3(b), except for the data of Sample Y05. The initial and

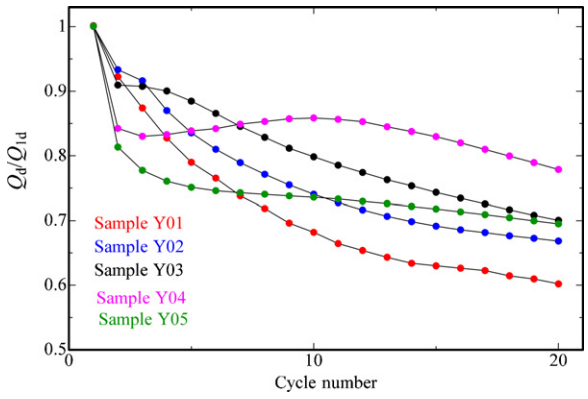

Fig. 8. Discharge capacity fading behavior at 30 °C with the cycle number for Li/Sample Y01–Y05 cells for 1.5–4.8 V under a fixed current density, 40 mA g^{-1}. All discharge capacities of each sample are normalized to initial one (Q_d/Q_{1d}) for easy comparison between samples.

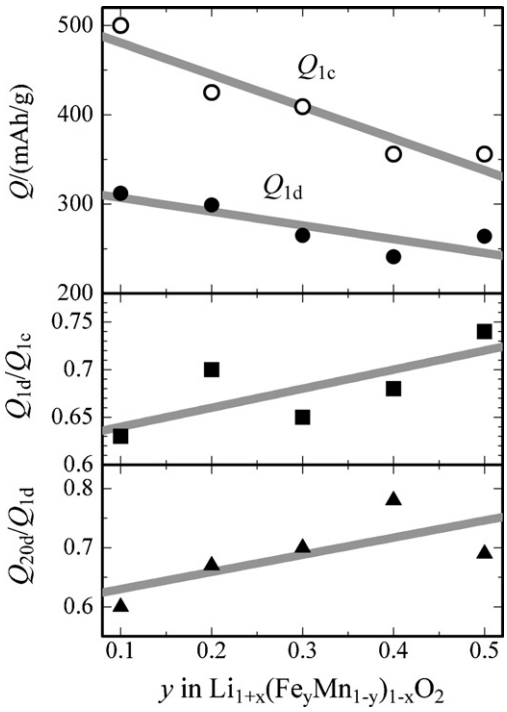

Fig. 9. The Fe content dependence on initial charge (Q_{1c}) and discharge (Q_{1d}) capacities (upper graph), efficiency (Q_{1d}/Q_{1c}) (middle one) and 20th discharge capacity retention (Q_{20d}/Q_{1d}, bottom one) for Li/Sample Y01–Y05 cells. Gray least-squares fit lines were included to depict the trend.

cycled discharge curve profiles were similar to those shown in Fig. 7 indicating that the trickle charging from 40 to 2 mA g^{-1} at 4.8 V is sufficient for Fe-substituted Li_2MnO_3.

Initial charge and discharge capacities (Q_{1c} and Q_{1d}), initial cycle efficiency (Q_{1d}/Q_{1c}) and 20th discharge capacity sustainability (Q_{20d}/Q_{1d}) values plotted against Fe content as shown in

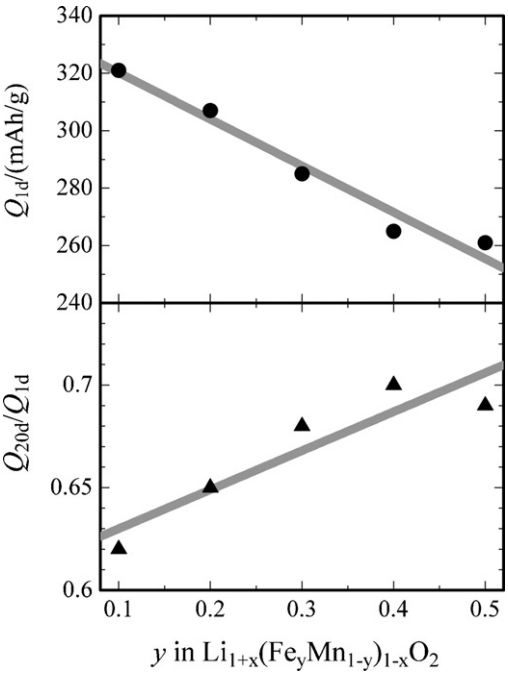

Fig. 10. The Fe content dependence on initial discharge (Q_{1d}) capacity (top graph), and 20th discharge capacity retention (Q_{20d}/Q_{1d}, bottom one) for Li/Sample Y01–Y05 cells. Gray least-squares fit lines were included to depict the trend.

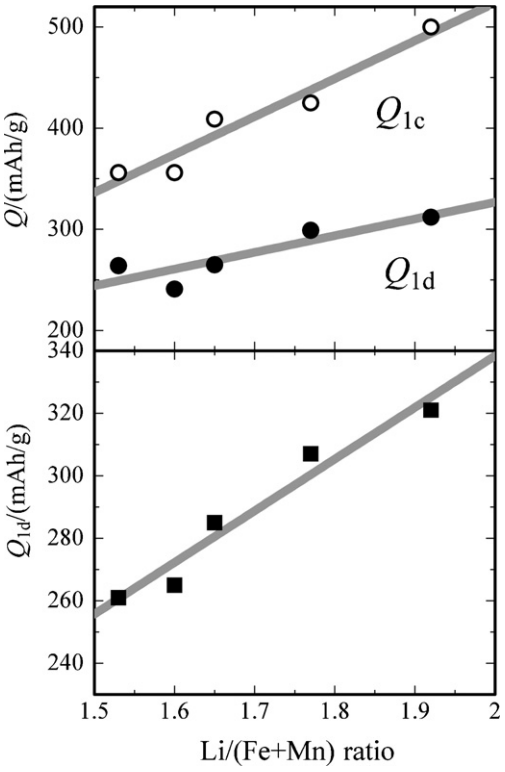

Fig. 11. Plots of initial charge (Q_{1c}) and discharge (Q_{1d}) capacities (top graph) and initial discharge (Q_{1d}) capacities (bottom one) against Li/(Fe + Mn) values for Li/Sample Y01–Y05 cells. Gray least-squares fit lines were included to depict the trend.

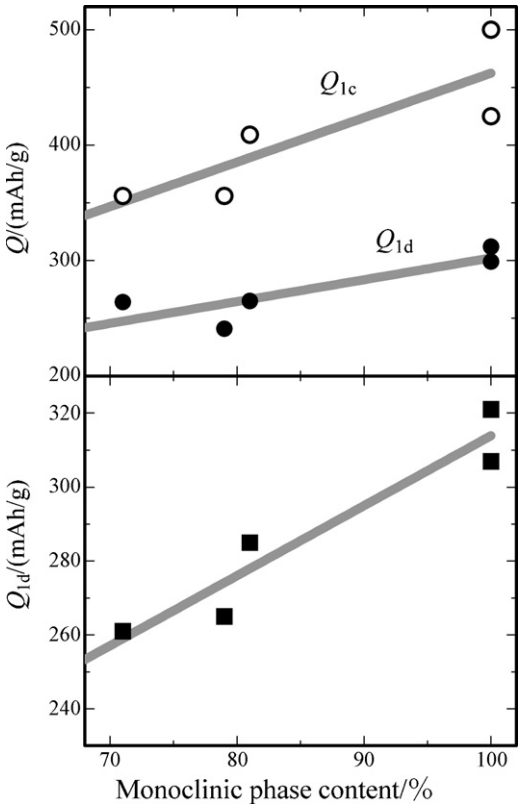

Fig. 12. Plots of initial charge (Q_{1c}) and discharge (Q_{1d}) capacities (top graph) and initial discharge (Q_{1d}) capacities (bottom one) against monoclinic phase contents for Li/Sample Y01–Y05 cells. Gray least-squares fit lines were included to depict the trend.

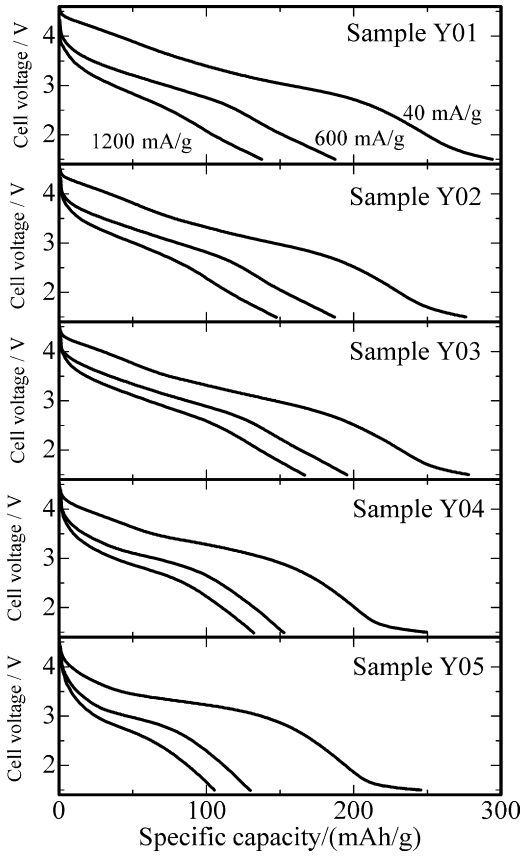

Fig. 13. Discharge curves at 30 °C from 4.8 to 1.5 V under a fixed current density, 40, 600, and 1200 mA g^{-1} for Li/Sample Y01–Y05 cells. The cell voltage was fixed at the upper voltage limit with decreasing current density until 2 mA g^{-1} only during the initial charging run.

Figs. 9 and 10. Despite initial charge condition, initial charge and discharge capacities decreased and initial cycle efficiency and 20th discharge capacity sustainability increased with increasing Fe content. The trend means that Fe incorporation into Li_2MnO_3 is considered to be effective at least from the viewpoint of initial cycle efficiency and discharge capacity sustainability. Initial charge and discharge capacities were found to depend on Li/(Fe + Mn) ratio (Fig. 11) and monoclinic phase content (Fig. 12). The results suggest that initial specific capacities of samples with high Fe content above 30% can be improved by raising Li content or minimizing cubic phase content.

The discharge curves and capacity under high current density from 40 to 3600 mA g^{-1} are shown in Fig. 13 and Table 4(a). The initial charge voltage was limited up to 4.8 V, as presented in Fig. 7. The discharge curves under high current density above 600 mA g^{-1} have different Fe content dependency from those at a moderate current density (40 mA g^{-1}). Increase in Fe content up to 30% reduced the capacity loss by changing current density from 40 to 600 mA g^{-1} and the samples with high Fe content above 30% reduced the capacity loss by changing current density from 600 to 1200 mA g^{-1}. These results mean that Fe is an effective element to improve high rate characteristics of Li_2MnO_3-based positive electrode material as well as Ni and Co.

Discharge characteristics at 0 and −20 °C were examined as presented in Fig. 14 and Table 4 (b). The initial charging to 500 mAh g^{-1} was selected. The difference in discharge capacity at 0 °C between samples with Fe content less than 30% is negligibly small and the discharge capacity at 0 °C decreased with increasing Fe content above 40%. Samples Y02–Y04 exhibited high discharge capacity (90–100 mAh g^{-1}) at −20 °C compared to those of other samples,

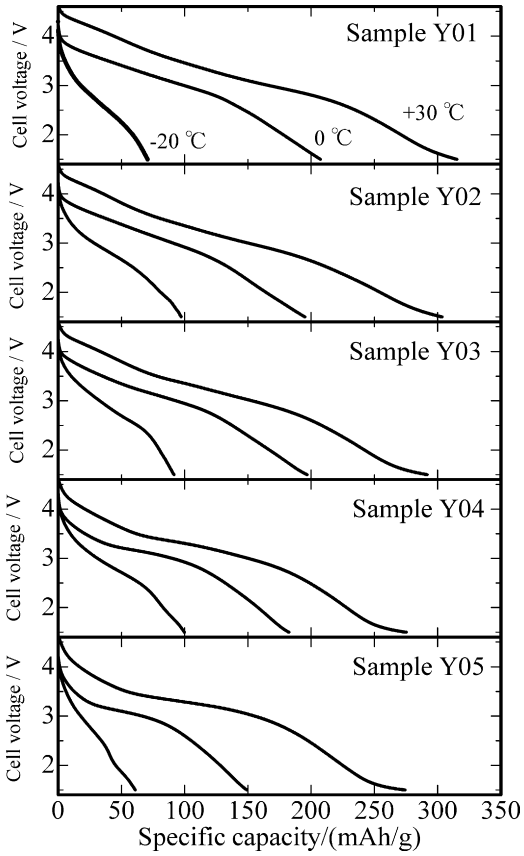

Fig. 14. Discharge curves under a fixed current density, 40 mA g^{-1} at 30, 0 and −20 °C for Li/Sample Y01–Y05 cells from 4.8 to 1.5 V. The initial charge capacity per active material was fixed at 500 mAh g^{-1} only.

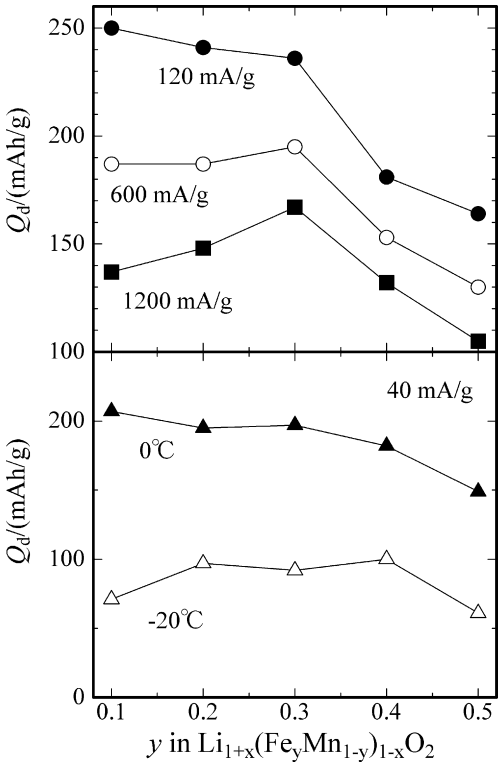

Fig. 15. The Fe content dependence on discharge (Q_d) capacity from 4.8 to 1.5 V under three different current densities, 120, 600 and 1200 mA g^{-1} at 30 °C (top graph), and under a two different temperatures, 0 and −20 °C at 40 mA g^{-1} (bottom one) for Li/Sample Y01–Y05 cells.

suggesting that Fe content per total cation content except for Li (20–40%) must be adjusted for optimization of low-temperature properties of Fe-substituted Li_2MnO_3. These electrochemical data include discharge characteristics under high current density, and for −20 °C, they reveal the important fact that Fe-substituted Li_2MnO_3 is still an attractive candidate as a positive electrode material.

To know what factors responsible for above high rate and low-temperature characteristics of this material, discharge capacity values under high current density or low temperature plotted against Fe content as shown in Fig. 15. The Fe content dependency was different from those under moderate current density at 30 °C in Figs. 9 and 10. The trend suggests that another factor except for Li/(Fe + Mn) ratio and monoclinic phase content is responsible for discharge characteristics under high current density or low temperature. The specific surface area (SSA) data was selected as a responsible factor as shown in Fig. 5, because the SSA data has different Fe content dependency from other two factors. The degree of contribution of SSA to discharge characteristics became large with increasing current density or decreasing operating temperature by

Table 4
Electrochemical charge and discharge characteristics between 1.5 and 4.8 V for Li/sample cells under different current density (a) and temperature at less than 30 °C at a fixed current density (b) during the discharging.

Sample	Discharge capacity under different current density/(mAh g^{-1})					
	40 mA g^{-1}	120 mA g^{-1}	600 mA g^{-1}	1200 mA g^{-1}	2400 mA g^{-1}	3600 mA g^{-1}
(a) Discharge capacity (Q_d) of cells discharged under high current density greater than 40–3600 mA g^{-1} at 30 °C after charging to 4.8 V at a fixed current density 40 mA g^{-1}. Charging was maintained at the upper limit voltage until reducing current density to 2.0 mA g^{-1} only during the initial charging run						
Sample Y01	294	250	187	137	83	60
Sample Y02	276	241	187	148	96	64
Sample Y03	278	236	195	167	118	87
Sample Y04	250	181	153	132	91	69
Sample Y05	246	164	130	105	72	58

Sample	Discharge capacity under different temperatures/(mAh g^{-1})		
	30 °C	0 °C	−20 °C
(b) Discharge capacity (Q_d) of cells discharged under different temperatures (30, 0 and −20 °C) after charging to 4.8 V at a fixed current density 40 mA g^{-1}. Charging was maintained up to 500 mAh g^{-1} only during the initial charging run			
Sample Y01	315	207	71
Sample Y02	304	195	97
Sample Y03	291	197	92
Sample Y04	275	182	100
Sample Y05	274	149	61

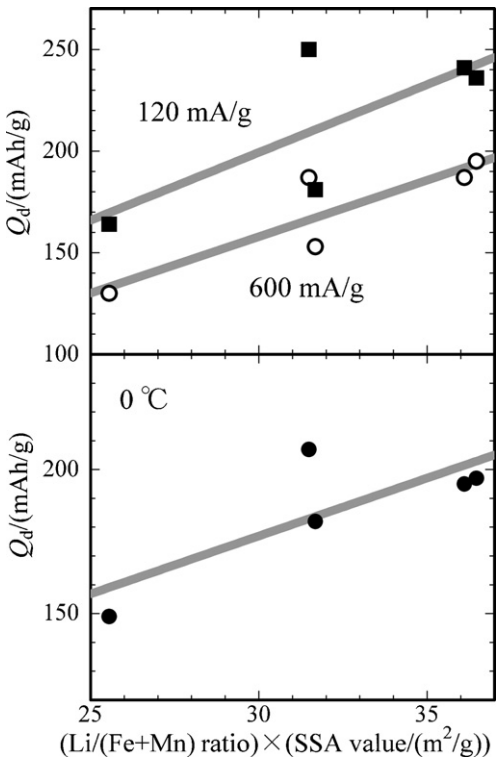

Fig. 16. Discharge (Q_d) capacities from 4.8 to 1.5 V under high current density, 120 and 600 mA g^{-1} at 30 °C (top graph), and moderate current density, 40 mA g^{-1} at 0 °C (bottom one) plotted against the product of Li/(Fe + Mn) ratio and BET specific surface area (SSA) value for Li/Sample Y01–Y05 cells. Gray least-squares fit lines are included to depict the trend.

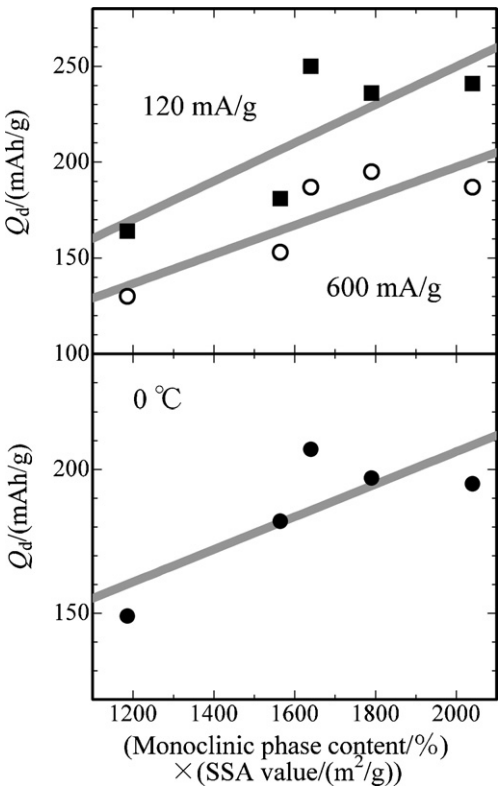

Fig. 17. Plots of discharge (Q_d) capacity from 4.8 to 1.5 V under high current density, 120 and 600 mA g^{-1} at 30 °C (top graph), and moderate current density, 40 mA g^{-1} at 0 °C (bottom one) against the product of monoclinic phase content and BET specific surface area (SSA) value for Li/Sample Y01–Y05 cells. Gray least-squares fit lines are included to depict the trend.

comparing the data in Fig. 15 with that in Fig. 5. The products of the SSA and Li/(Fe + Mn) ratio or monoclinic phase content were plotted against discharge capacity less than 600 mA g^{-1} and at 0 °C as shown in Figs. 16 and 17, respectively. Both figures indicate that the sample consisted of fine particles with high Li/(Fe + Mn) ratio or high monoclinic phase content is needed to improve the discharge characteristics under high current density less than 600 mA g^{-1} or below room temperature down to 0 °C.

To explain the Fe content dependency of discharge characteristics under high current density above 1200 mA g^{-1} or that at −20 °C, discharge capacity values above 1200 mA g^{-1} and at −20 °C were plotted against corresponding SSA data as shown in Fig. 18. Linear dependency with positive gradient was obtained, indicating that discharge characteristics under high current den-

Table 5
Relation between sample nature factors and electrochemical performance for Fe-substituted Li_2MnO_3 positive electrode material.

Factors originated from sample nature	Responsible electrochemical data
Fe content, Fe/(Fe + Mn)	• Initial charge voltage ↓ • Initial charge and discharge capacity ↓ • Initial efficiency ↑ • Cycle performance↑ (Fe/(Fe + Mn) < 40%)
Li/(Fe + Mn) ratio and monoclinic (*C*2/*m*) phase content	• Initial charge and discharge capacity ↑
Specific surface area	• Discharge capacity ↑ (<600 mA g^{-1} or >0 °C) • Discharge capacity ↑ (>120 mA g^{-1} or <0 °C)

Arrows indicate tendency of change in electrochemical parameters when focused sample nature factor is increased. The "upward" and "downward" arrows mean "increase" and "decrease" monotonously with increasing focused sample nature factor value, respectively.

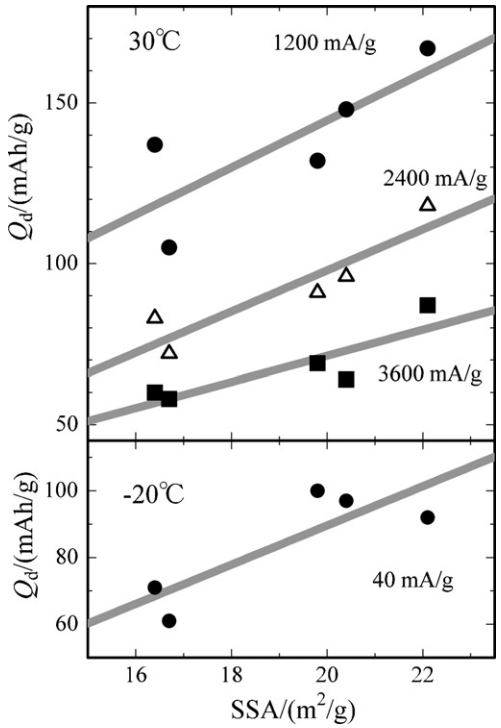

Fig. 18. Plots of discharge (Q_d) capacity from 4.8 to 1.5 V under high current density, 1200 (closed circle), 2400 (open triangle) and 3600 mA g^{-1} (closed square) at 30 °C (top graph), and moderate current density, 40 mA g^{-1} at −20 °C (bottom one) against the BET specific surface area (SSA) value for Li/Sample Y01–Y05 cells. Gray least-squares fit lines are included to depict the trend.

sity above 1200 mA g^{-1} or that at −20 °C were governed mainly by power character. High rate and low-temperature characteristics of this material depend on not only the compositional and structural factors (Li/(Fe + Mn) ratio and monoclinic phase content) but also the power parameter (SSA). The involvement of SSA term to the electrochemical property lead to the importance of preparation technique of the Li_2MnO_3-based positive electrode material. In fact, the specific surface area affects the electrochemical property of Li_2MnO_3 [28]. Although our wet-chemical method (coprecipitation–hydrothermal–calcination method) is a good candidate as preparation technique, further efforts must be needed to make the samples composed of uniform Fe and Mn distribution and fine particles with high Li/(Fe + Mn) ratio, monoclinic content and specific surface area values.

4. Conclusion

Positive electrode materials of Fe-substituted Li_2MnO_3 with different Fe contents of 10–50% were prepared using wet-chemical preparation methods, including hydrothermal processing. All samples had high initial specific capacity greater than 200 mAh g^{-1}. For optimized iron contents of less than 20%, the initial discharge capacity reached 300 mAh g^{-1}. As described in the earlier sections of this report, many factors should be controlled to optimize the electrochemical properties of Fe-substituted Li_2MnO_3. The relation between four factors of sample nature and electrochemical properties is summarized in Table 5. The Fe content dominates mainly the initial charge voltage, initial charge and discharge capacities, initial efficiency, and cycle performance. High Fe contents greater than 30% in the sample contribute to suppression of a change in the shape of the discharge curve and better cycle stability.

The Li/(Fe + Mn) ratio and monoclinic phase content influence not only electrochemical property at room temperature under moderate current density but also the discharge characteristics under high current density and below room temperature. The specific surface area term should be considered to improve the discharge characteristics under high current density and below room temperature. Although further efforts to improve electrochemical properties are needed, Fe-substituted Li_2MnO_3 is an attractive 3 V class positive electrode material for use as a rechargeable lithium battery because it consists of inexpensive elements, Fe and Mn are obtainable from abundant natural sources.

Acknowledgements

MT expresses his gratitude to Ms. Hideka Shibuya and Mr. Yusuke Maeda of Tanaka Chemical Corporation for chemical analysis and specific surface area measurement and to Prof. Tatsuya Nakamura of the University of Hyogo for fruitful discussions. This study was supported financially by a national project (Li-EAD project) of the Ministry of Economy, Trade and Industry (METI) and the New Energy and Industrial Technology Development Organization (NEDO).

References

[1] P. Kalyani, S. Chitra, T. Mohan, S. Gopukumar, J. Power Sources 80 (1999) 103–106.
[2] A.D. Robertson, P.G. Bruce, Chem. Commun. (2002) 2790–2791.
[3] C.S. Johnston, J.-S. Kim, C. Lefief, N. Li, J.T. Vaughey, M.M. Thackeray, Electrochem. Commun. 6 (2004) 1085–1091.
[4] B. Ammundsen, J. Paulsen, Adv. Mater. 13 (2001) 943–956.
[5] K. Numata, C. Sakaki, S. Yamanaka, Chem. Lett. 26 (1997) 725–726.
[6] T. Ohzuku, Y. Makimura, Chem. Lett. 30 (2001) 744–745.
[7] Z. Lu, D.D. MacNeil, J.R. Dahn, Electrochem. Solid State Lett. 4 (2001) A191–A194.
[8] B. Ammundsen, J. Paulsen, I. Davidson, R.-S. Liu, C.-H. Shen, J.-M. Chen, L.-Y. Jang, J.-F. Lee, J. Electrochem. Soc. 149 (2002) A431–A436.
[9] Z. Lu, J.R. Dahn, J. Electrochem. Soc. 149 (11) (2002) A1454–A1459.
[10] Y.J. Park, Y.-S. Hong, X. Wu, M.G. Kim, K.S. Ryu, S.H. Chang, J. Electrochem. Soc. 151 (2004) A720–A727.
[11] Z. Lu, L.Y. Beaulieu, R.A. Donaberger, C.L. Thomas, J.R. Dahn, J. Electrochem. Soc. 149 (2002) A778–A791.
[12] W.-S. Yoon, Y. Paik, X.-Q. Yang, M. Balasubramanian, J. McBeen, C.P. Grey, Electrochem. Solid-State Lett. 5 (2002) A263–A266.
[13] R. Armstrong, M. Holzapfel, P. Novák, C.S. Johnson, S.-H. Kang, M.M. Thackeray, P.G. Bruce, J. Am. Chem. Soc. 128 (2006) 8694–8698.
[14] T.A. Arunkumar, Y. Wu, A. Manthiram, Chem. Mater. 19 (2007) 3067–3073.
[15] C.S. Johnson, N. Li, C. Lefief, J.T. Vaughey, M.M. Thackeray, Chem. Mater. 20 (2008) 6095–6106.
[16] M.M. Thackeray, S. Kang, C.S. Johnston, J.T. Vaughey, R. Benedek, S.A. Hackney, J. Mater. Chem. 17 (2007) 3112–3125.
[17] N. Tran, L. Croguennec, M. Ménétrier, F. Weill, P. Biensan, C. Jordy, C. Delmas, Chem. Mater. 20 (2008) 4815–4825.
[18] M. Tabuchi, H. Shigemura, K. Ado, H. Kobayashi, H. Sakaebe, H. Kageyama, R. Kanno, J. Power Sources 97–98 (2001) 415–419.
[19] M. Tabuchi, A. Nakashima, H. Shigemura, K. Ado, H. Kobayashi, H. Sakaebe, H. Kageyama, T. Nakamura, M. Kohzaki, A. Hirano, R. Kanno, J. Electrochem. Soc. 149 (2002) A509–A524.
[20] M. Tabuchi, A. Nakashima, K. Ado, H. Kageyama, K. Tatsumi, Chem. Mater. 17 (2005) 4668–4677.
[21] M. Tabuchi, A. Nakashima, K. Ado, H. Sakaebe, H. Kobayashi, H. Kageyama, K. Tatsumi, Y. Kobayashi, S. Seki, A. Yamanaka, J. Power Sources 146 (2005) 287–293.
[22] M. Tabuchi, Y. Nabeshima, M. Shikano, K. Ado, H. Kageyama, K. Tatsumi, J. Electrochem. Soc. 154 (2007) A638–A648.
[23] M. Tabuchi, Y. Nabeshima, K. Ado, M. Shikano, H. Kageyama, K. Tatsumi, J. Power Sources 174 (2007) 554–559.
[24] J. Kikkawa, T. Akita, M. Tabuchi, K. Tatsumi, M. Kohyama, Appl. Phys. Lett. 91 (2007) 054103.
[25] J. Kikkawa, T. Akita, M. Tabuchi, M. Shikano, K. Tatsumi, M. Kohyama, J. Appl. Phys. 103 (2008) 104911.
[26] J. Kikkawa, T. Akita, M. Tabuchi, M. Shikano, K. Tatsumi, M. Kohyama, Electrochem. Solid-State Lett. 11 (2008) A183–A186.
[27] Y. Koyama, I. Tanaka, M. Nagao, R. Kanno, J. Power Sources 189 (2009) 798–801.
[28] D. Yu, K. Yanagida, K. Kato, H. Nakamura, J. Electrochem. Soc. 156 (2009) A417–A424.
[29] M. Tabuchi, K. Tatsumi, S. Morimoto, S. Nasu, T. Saito, Y. Ikeda, J. Appl. Phys. 104 (2008) 043909.
[30] F. Izumi, T. Ikeda, Mater. Sci. Forum. 321–324 (2000) 198–203.
[31] P. Strobel, B. Lambert-Andron, J. Solid State Chem. 75 (1988) 90–98.
[32] J.C. Anderson, M. Schieber, J. Phys. Chem. Solids 25 (1964) 961–968.
[33] P.S. Whitfield, I.J. Davidson, P.W. Stephens, L.M.D. Cranswick, I.P. Swainson, Z. Kristallogr. Suppl. 26 (2007) 483–488.
[34] Z. Lu, J.R. Dahn, J. Electrochem. Soc. 149 (2002) A815–A822.
[35] C.S. Johnston, N. Li, J.T. Vaughey, S.A. Hackney, M.M. Thackeray, Electrochem. Commun. 7 (2005) 528–536.
[36] A.D. Robertson, P.G. Bruce, Chem. Mater. 15 (2003) 1984–1992.
[37] N. Kumagai, J. Kim, S. Tsuruta, Y. Kadoma, K. Ui, Electrochim. Acta 53 (2008) 5287–5293.
[38] M.M. Thackeray, Prog. Solid State Chem. 25 (1997) 1–71.